

Comparison of Soil Thickness in a Zero-Order Basin in the Oregon Coast Range Using a Soil Probe and Electrical Resistivity Tomography

Michael S. Morse¹; Ning Lu, F.ASCE²; Jonathan W. Godt³; André Revil⁴; and Jeffrey A. Coe⁵

Abstract: Accurate estimation of the soil thickness distribution in steepland drainage basins is essential for understanding ecosystem and subsurface response to infiltration. One important aspect of this characterization is assessing the heavy and antecedent rainfall conditions that lead to shallow landsliding. In this paper, we investigate the direct current (DC) resistivity method as a tool for quickly estimating soil thickness over a steep (33–40°) zero-order basin in the Oregon Coast Range, a landslide prone region. Point measurements throughout the basin showed bedrock depths between 0.55 and 3.2 m. Resistivity of soil and bedrock samples collected from the site was measured for degrees of saturation between 40 and 92%. Resistivity of the soil was typically higher than that of the bedrock for degrees of saturation lower than 70%. Results from the laboratory measurements and point-depth measurements were used in a numerical model to evaluate the resistivity contrast at the soil-bedrock interface. A decreasing-with-depth resistivity contrast was apparent at the interface in the modeling results. At the field site, three transects were surveyed where coincident ground truth measurements of bedrock depth were available, to test the accuracy of the method. The same decreasing-with-depth resistivity trend that was apparent in the model was also present in the survey data. The resistivity contour of between 1,000 and 2,000 Ωm that marked the top of the contrast was our interpreted bedrock depth in the survey data. Kriged depth-to-bedrock maps were created from both the field-measured ground truth obtained with a soil probe and interpreted depths from the resistivity tomography, and these were compared for accuracy graphically. Depths were interpolated as far as 16.5 m laterally from the resistivity survey lines with root mean squared error (RMSE) = 27 cm between the measured and interpreted depth at those locations. Using several transects and analysis of the subsurface material properties, the direct current (DC) resistivity method is shown to be able to delineate bedrock depth trends within the drainage basin. DOI: [10.1061/\(ASCE\)GT.1943-5606.0000717](https://doi.org/10.1061/(ASCE)GT.1943-5606.0000717). © 2012 American Society of Civil Engineers.

CE Database subject headings: Soil properties; Slope stability; Unsaturated soils; Site investigation; Oregon; Radiography.

Author keywords: Direct current resistivity; Soil thickness; Slope stability; Unsaturated soils; Site characterization.

Introduction

Direct monitoring of pore-water response to rainfall and estimation of the variability of soil thickness in steepland drainage basins are essential for understanding the conditions leading to shallow landslide initiation (e.g., Godt et al. 2009; Montgomery et al. 2009). Shallow landslides are an important part of the erosion process and

a persistent hazard in mountainous areas, particularly in wet climates where shallow slides may be triggered by a combination of heavy storm and antecedent rainfall (Dai and Lee 2001; Kim et al. 2004; Lu and Godt 2008) or where the contact between colluvial soil and underlying bedrock is abrupt (e.g., Campbell 1975).

The Oregon Coast Range is susceptible to shallow landslides because of steep topography, heavy rainfall, and human land use activities associated with timber harvesting (e.g., Brown and Krygier 1971; Pierson 1977; Montgomery et al. 2000). Recent work in the area on shallow landsliding and debris-flow initiation has focused on the influence of vegetation roots on slope stability (Schmidt et al. 2001; Roering et al. 2003) and the role of pore-water response from rainfall in soil and shallow bedrock in triggering landslides (Wu and Sidle 1995; Montgomery et al. 1997; Torres et al. 1998). At a site near Coos Bay, Oregon, Montgomery et al. (2009) collected extensive monitoring data to characterize the subsurface pore pressures leading to the onset of landsliding and highlighted the influence of flow from fractured weathered bedrock in generating pore pressures in the overlying soil during a heavy rainstorm. An important constraint on groundwater and slope-stability modeling of the site (Ebel et al. 2008, 2010) was the depth of the interface between the soil and the underlying bedrock, which for these modeling studies was painstakingly measured by hand (Schmidt 1999).

Because geophysical techniques offer a means to image variation in subsurface materials at the hillslope and basin scale, they are increasingly used in landslide investigations. Bogoslovsky and Ogilvy (1977) outlined the effectiveness of using nonintrusive geophysical

¹Graduate Student, Hydrologic Science and Engineering, Colorado School of Mines, Golden, CO 80401. E-mail: mmorse@mines.edu

²Professor, Dept. of Civil and Environmental Engineering, Colorado School of Mines, Golden, CO 80401 (corresponding author). E-mail: ninglu@mines.edu

³Research Physical Scientist, Geologic Hazards Science Center, U.S. Geological Survey, Denver, CO 80225. E-mail: jgodt@usgs.gov

⁴Associate Professor, Dept. of Geophysics, Colorado School of Mines, Golden, CO 80401; and Professor, Institut des Sciences de la Terre, Centre National de la Recherche Scientifique, Unite Mixte de Recherche 5275, Université de Savoie, 73376 cedex, Le Bourget du Lac, France. E-mail: arevil@mines.edu

⁵Research Geologist, Geologic Hazards Science Center, U.S. Geological Survey, Denver, CO 80225. E-mail: jcoe@usgs.gov

Note. This manuscript was submitted on July 16, 2010; approved on February 27, 2012; published online on March 1, 2012. Discussion period open until May 1, 2013; separate discussions must be submitted for individual papers. This paper is part of the *Journal of Geotechnical and Geoenvironmental Engineering*, Vol. 138, No. 12, December 1, 2012. ©ASCE, ISSN 1090-0241/2012/12-1470-1482/\$25.00.

tools to study landslides, specifically, because a large number of repeat measurements can be made with minimal effort. The direct current (DC) resistivity method is an increasingly popular tool that can be used to characterize the shallow subsurface geology for problems in geomorphology (e.g., Schrott and Sass 2008). Bichler et al. (2004) conducted an extensive study using DC resistivity, seismic reflection and refraction, and ground-penetrating radar to create a three-dimensional (3D) map of a landslide slip surface. Schmutz et al. (2009) used resistivity and time-domain electromagnetics to obtain a 3D subsurface map of an earthflow in the Alps. Lapenna et al. (2003) used resistivity and self-potential to map the boundaries of a landslide in southern Italy.

Only recently has the DC resistivity method been applied to the vadose zone (Friedel et al. 2006), and little work has been done to accurately distinguish subsurface structures and create a basin-scale assessment of the shallow soil-bedrock contact using this technique. Because of the nonunique solutions typical of many geophysical studies, most studies have employed more than one geophysical technique to characterize subsurface geology on hillslopes (e.g., Lapenna et al. 2003; Bichler et al. 2004; Schmutz et al. 2009).

In this study, we conducted a shallow DC resistivity survey of a steep-land drainage basin in the Oregon Coast Range. Inversions of the geophysical data were conducted to produce resistivity tomograms for each transect. Electrical resistivity of soil and bedrock samples collected from the site was measured in the laboratory, and the electrical contrast between the soil and bedrock was further studied using 2D forward modeling. Bedrock depths were then determined in the DC survey tomograms, and an interpolated depth map for the basin was created using geostatistics. The results were compared with existing point measurements of bedrock depth from boreholes to assess the validity of the DC resistivity method as a means of determining bedrock depth throughout the drainage

basin. This study demonstrates that DC resistivity is sufficient for mapping the soil-bedrock contact surface geometry if the material properties are well characterized.

Site Description

The study site is a southwest-facing zero-order basin located within the Elliott State Forest ~20 km southeast of Reedsport in the Oregon Coast Range (Fig. 1). Zero-order basins are steep, unchanneled swales or bedrock hollows and are the uppermost catchments in a stream network (Dietrich and Dunne 1978; Benda 1990; Benda et al. 2005). Because colluvium tends to collect in the hollow axis, and bedrock topography tends to focus groundwater flow, zero-order basins are often the locus for shallow landslides (e.g., Dietrich et al. 1986). We selected this particular location because of its steep topography (33–40°) and the recent (~3 years prior to the geophysical survey) removal of trees from the basin for commercial timber harvest, factors that contribute to the potential for shallow landslides (e.g., Schmidt et al. 2001; Sidle and Ochiai 2006).

The surface of the basin is covered with tree stumps and woody debris in various states of decomposition left after logging (Fig. 2). At the time of the study, the majority of surface vegetation was comprised of dispersed patches of rhododendron and 3-year-old Douglas fir saplings planted after clear-cut harvest. Irregularities in the slope topography suggested the presence of deposits resulting from slumping and small-scale (5 m wide) landslides, particularly near the head of the basin. Outcrops of massive Tertiary sandstone, interbedded with siltstone and mudstone, occur locally on ridgelines and roadcuts and compose the bedrock underlying the field site. A study by Lovell (1969), which described the materials of the Tyece basin in the area of the field site as composed of ~95% sandstone

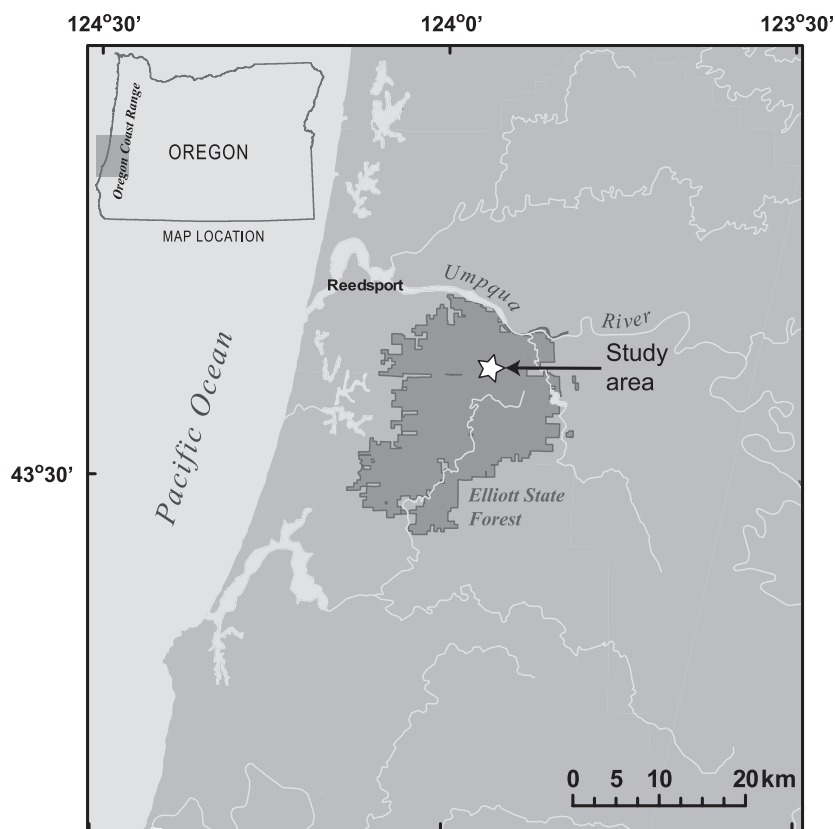


Fig. 1. Map showing location of the field site within the Oregon Coast Range in the Elliott State Forest

with the remaining 5% composed of siltstone and shale. Outcrops of the sandstone beds near the field site generally dipped to the southwest at an angle of 9°. At the time of the geophysical survey, soil moisture conditions at the site were dry with no recorded precipitation for the week before the survey—typical conditions for the Oregon Coast Range in the summer season.

We identified four distinct subsurface units within soil profiles at the site (Fig. 3). The top layer (0–20 cm) is an organic rich horizon (O soil horizon; Birkeland 1999) composed of mostly of black duff and roots. Below this layer (10–60 cm) is a thick dark brown to black soil with ~5% tan clasts with some 5-cm-diameter macropores and decomposing and intact roots (A and weak B soil horizons). Farther down (60–100 cm) is a layer of brown, cobbly, slightly sticky sand with ~30% weathered clasts (C soil horizon). Beneath the brown layer is a hard, tan to reddish-tan, weathered sandstone (100–120 cm; Cr soil horizon). Wood and remnant roots in the subsurface are shown as bright objects in the photo. Similar structures were found in soil pits near other boreholes. The sapling in the foreground was manually planted 3 years after clear-cut harvest.



Fig. 2. Surface vegetation and remnant stumps at survey site; location is in drainage basin axis, facing directly upslope

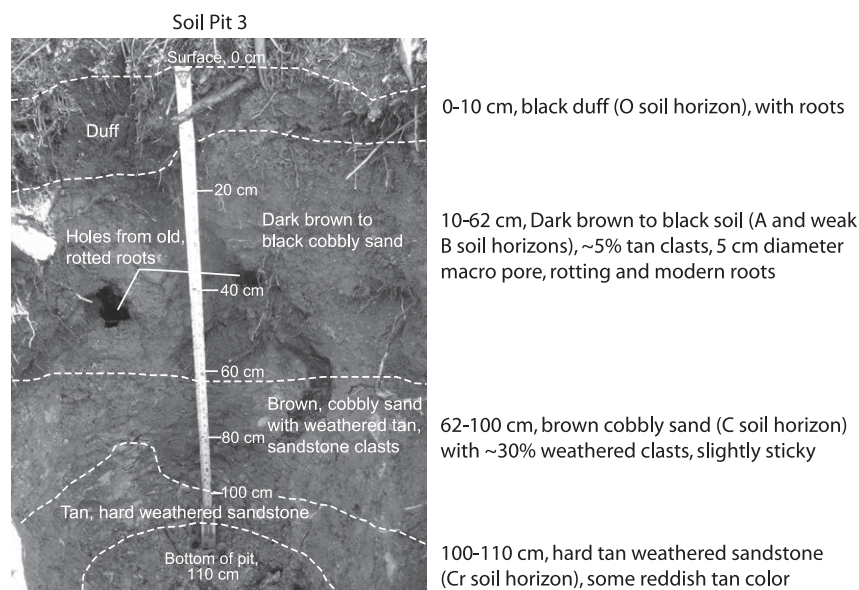


Fig. 3. Soil pit near GP1; soil horizon designations follow the nomenclature of Birkeland (1999)

Methods

Bedrock Depth and Topographic Survey

A total of thirty soil thickness measurements were taken using a 2.5-cm-diameter soil probe at locations throughout the basin (Fig. 4). Spatial variability of elevation and depth was calculated using a kriging method. Soil thickness measurements are marked by SD#; boreholes are marked by GP#. Location of each geophysical survey line at the site is shown: upslope survey, A-A'; downslope survey, B-B'; axis survey, C-C'. The hand-driven soil probe removed cores of material in 30-cm runs to a maximum depth of 1.8 m. Soil-bedrock contact depths were determined from the observed change of color in the extracted cores, and at depths where further progress was impeded. Three larger (5.6 cm diameter) boreholes were completed at locations along the catchment axis with a Geoprobe MC-5* sampler and demolition hammer. The Geoprobe sampler retrieved intact cores of the soil and bedrock and was capable of coring to a maximum depth of 6 m. Bedrock depths were determined with the same method as with the hand probe. Soil pits of ~4 ft in diameter were also dug to the depth of the soil-bedrock contact at each Geoprobe borehole location, to better describe the soil profile and collect soil samples.

Surface topography of the study site was surveyed using a total station. Elevation measurement points were spread randomly to obtain topographic trends over the catchment area. Locations of the bedrock depth measurements were also surveyed. Global positioning system data with 2-cm resolution were obtained for two control points, so that total station data could be transformed to the Universal Transverse Mercator (UTM) coordinate system. Kriging of the surface topography and soil depth data was performed using the geostatistics software, Surfer 9, to create a topographic contour map and a depth-to-bedrock map of the basin (Fig. 4). The data from the kriged grids illustrated in Fig. 4 were used to guide the geophysical investigation discussed in the next section.

Geophysical Survey

Electrical conductivity represents the ability of a material to conduct electrical current and is the inverse of electrical resistivity. The

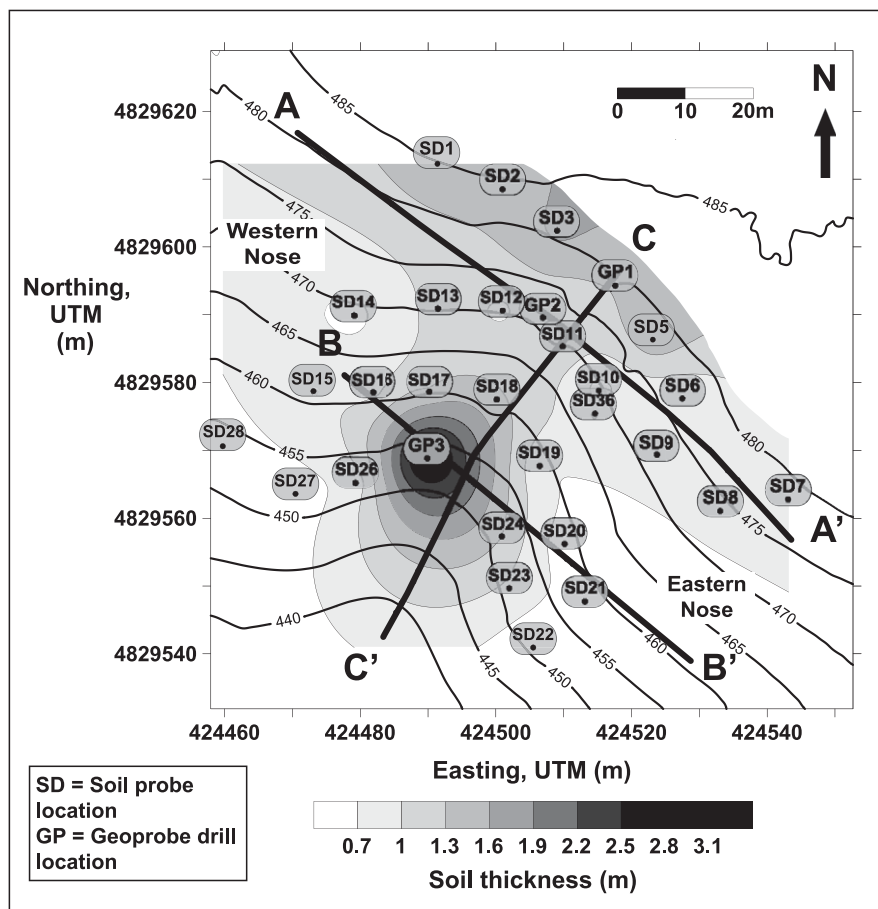


Fig. 4. Map showing surface topography and soil thickness determined from field measurements at study site

DC resistivity method was used to obtain a laterally continuous tomogram of subsurface resistivity. Electrical conductivity of a porous soil or rock depends on a number of properties including porosity, tortuosity of the pore space, total dissolved solids in the pore water solution, water content, temperature, cation exchange capacity of the material, and frequency of electrical current (Revil et al. 1998; Revil and Glover 1998). When the cation exchange capacity of the porous material is negligible, the electrical conductivity, σ , can be related to the porosity, ϕ , and the level of relative saturation, S_w , in the pores (Archie 1942) by

$$\sigma = \sigma_w S_w^n \phi^m \quad (1)$$

where σ_w = conductivity of water, and m and n = first and second Archie exponents, respectively.

Apparent resistivity data were obtained with an Advanced Geosciences Inc. (AGI) Super Sting R1 resistivity meter. The resistivity meter internally calculated the apparent resistivity in the field based on the array type, spacing, and induced current for a subsurface half-space. Accuracy of the field measurements was optimized by implementing several “cycles”—or intervals of applied current and subsequent voltage readings—with the instrument. We used a Wenner- α (constant spacing) type array because of its favorable signal-to-noise ratio and propensity for detecting horizontal layers in the subsurface.

Three resistivity transects were surveyed at the site (Fig. 4). Two transects (upslope transect, A-A'; downslope transect, B-B') were oriented perpendicular to the basin axis. The upslope transect extended a total of 98 m, and the downslope transect extended 67.2 m.

An additional survey line (axis transect, C-C') ran along the basin axis, extending a total of 80 m. For the upslope and downslope transects, an electrode spacing of 0.7 m was used; and for the axis transect, the spacing was 1.0 m. The electrode spacing was determined to obtain an optimal density of data for a subsurface depth up to 2.0 m. The target depth for each survey was designed to be consistent with the bedrock depths obtained from the soil probe measurements for maximal density of data points around the contact for the purpose of this study. Prior knowledge of the approximate bedrock contact depth allows for the use of electrode spacings that yield the greatest resolution of resistivity data at that depth, thereby increasing the efficiency of the geophysical survey and the quality of data.

Laboratory Resistivity Measurements

Understanding the electrical properties of the soil and bedrock at the field site is needed to interpret a resistivity contrast in the tomography data. Because of the nonunique result of a field geophysical survey, the materials in question should be properly characterized with supplementary data or through experiments conducted in a controlled setting. We obtained soil samples from pits dug near the Geoprobe borehole locations GP1 and GP3 (Fig. 4) at the field site. Soil was procured using a shovel and bucket, and depth of the sampling was recorded. One sandstone sample was removed from an outcrop at the top of a local ridgeline. Water samples were taken from the confluence of two drainages downslope from the field site, to measure the conductivity of the pore water in the basin used to solve for Eq. (1).

The soil samples were first dried in an oven and weighed; then tap water was added, by weight, to the target degree of saturation

for the resistivity experiments. The moist soil was then compacted in a plastic box that measured 30.4 cm length \times 15.4 cm width \times 7.0 cm height. A compaction hammer was dropped from a uniform height to compact each sample to a porosity of 0.42. The soil was covered and cured for one hour, to equilibrate the moisture content within the pore structure. The sample was then weighed after each measurement, to account for the loss of water mass as the result of evaporation.

We used an ABEM Terrameter SAS4000 to induce a current through the compacted soil sample and simultaneously measure the resistance. Four copper electrodes in a Wenner- α type array were placed in a uniform spacing of 7.5 cm in the soilbox experiments. The method of measurement for the soil resistance was similar to those conducted at the field site, where two electrodes apply the current, and two electrodes measure the voltage drop. However, because the confined laboratory experiments were not conducted in an infinite half-space, a geometric factor was required to solve for the electrical resistivity of the soil at the given degree of saturation.

We calculated the resistivity for the experimental soil box data, by creating a model of the experimental setup using COMSOL Multiphysics 3.5. COMSOL Multiphysics is a finite element analysis that can be used to solve the Laplace equation for the electrical potential distribution for a given geometry, resistivity distribution, and position of the two current and the two potential electrodes. We calculated the resistivity of the soil at different degrees of saturation using the geometric factor in COMSOL model.

The electrical properties of the sandstone specimen were measured using an impedance meter working in the frequency domain (for details, see Leroy et al. 2008 and Jougnot et al. 2010). The sample was dried in an oven, and the porosity was determined to be 0.35 using a simple buoyancy test. The dry sample was then submerged until a degree of saturation of 75% was reached, determined by weighing the sample before and after submersion. The saturation was to ensure the electrical current density distribution would be uniform throughout the volume of media. A sine wave of current was applied through the two current electrodes through the material at discrete frequencies, to measure both the resulting amplitude (potential) and phase lag of the wave at two potential electrodes. The sample was chiseled into a block with a known length of 23 cm, width of 16 cm, and height of 15 cm, to find the geometrical factor of the sample (Niininen and Kelha 1979). The electrode array was a Wenner- α with a spacing of 3 cm. The resulting complex impedance was converted to a complex resistivity using the geometrical factor determined from finite-element software, and the resistivity was determined at the frequency used for the field investigation (~ 10 Hz).

Inverse and Forward Modeling

Electrical resistivity tomography was performed with the RES2DINV program (Loke and Barker 1996), using the robust L_1 norm optimization method (Claerbout and Muir 1973; Wolke and Schwetlick 1988). The robust inversion method is preferable for problems with sharp boundaries between two layers of differing resistivities because it implements a damping factor that permits greater value disparity for regions around the contact (Ellis and Oldenburg 1994). Implementation of the damping factor required ground-truth information on the bedrock contact, to delineate the expected depth for the layer boundary. In addition to the observed sharp resistivity contrast, the robust inversion method was preferable for this study in order to obtain the best model of the resistivity variations at the soil–bedrock contact and to mitigate the erratic data obtained from macropores (soil pipes), irregular geometry of the bedrock contact, bedrock clasts, and roots in the shallow subsurface (Claerbout and Muir 1973).

Results from the laboratory measurements were used to develop a two-layer, 2D forward model of each survey transect. We used the RES2DMOD forward modeling software for its ease of integration with the aforementioned inversion software. RES2DMOD simulates a field resistivity pseudosection using the finite-difference method to calculate the apparent resistivity distribution for a user-defined mesh (Loke 1999). The user also defines a specific resistivity value to the individual mesh squares. Resistivity values measured for the soil and bedrock in the laboratory were assigned to the mesh in the forward model. Elevations of the electrode locations used for the field geophysics survey were measured with the total station survey and input to the forward model domain. Noise of $\sim 1\%$ was added to the dataset, to mimic the instrument error of the resistivity at the field site. The same robust method of inversion was used to create tomograms for the forward model that were compared with those created from the geophysical survey. The inverse solution of the forward modeling was used to help recognize the resistivity transition at the soil–bedrock contact in the geophysical data.

Results

Point Measurement Survey

Fig. 4 shows the bedrock depth distribution determined from the direct soil depth measurements, overlain with locations for the DC resistivity survey transects. Soil profiles increase in thickness toward the basin axis and decrease toward the local basin boundaries where probe location SD20 registered the shallowest depth to bedrock at 0.55 m. Bedrock depth also increases with distance downslope along the axis, where the thickest measured soil profile extends to a maximum depth of 3.1 m at borehole GP3. Samples procured at 3.1 m in borehole GP3 were saturated with water and represent the only encounter with a possible water table at the time of this study (July 2009). We located the local water table near the basin axis at a downslope location (GP3), and assumed that the moisture content profile of the soil above the bedrock does not vary significantly from axis to nose.

Laboratory Measurements

Fig. 5 shows the results from the direct resistivity measurements of the soil and bedrock samples performed in the laboratory. Results of the soil resistivity were experimentally derived, whereas the sandstone resistivity distribution was determined using Archie's law [Eq. (1)]. A maximum degree of saturation of 92% was used in the experiment for both soils. Electrical conductivity of the added tap water was measured to be a consistent 3.9×10^{-2} S/m at 21°C, which was similar to the measured conductivity of the water obtained downslope from the study site (2.1×10^{-2} S/m). The soil sample obtained from the pit near GP1 (Fig. 4) was poorly sorted, whereas the soil from GP3 was more homogenous in grain size. Values from the sandstone experiment were extrapolated using Archie's second law. We estimated the Archie exponents for the sandstone in Eq. (1) to be $m = n = 2$, based on the typical values observed for clean, consolidated sandstone (Archie 1942). Because the porosity of the specimen and the electrical conductivity of the water were known, resistivity was estimated for different values of saturation using Eq. (1).

The resistivity values calculated using Archie's second law for the sandstone with a degree of saturation between 40 and 50% was between 1,000 and 2,000 Ω m. As shown in Fig. 5, the difference between the resistivity of the sandstone and the two soils decreases as the level of water saturation increases to $>70\%$.

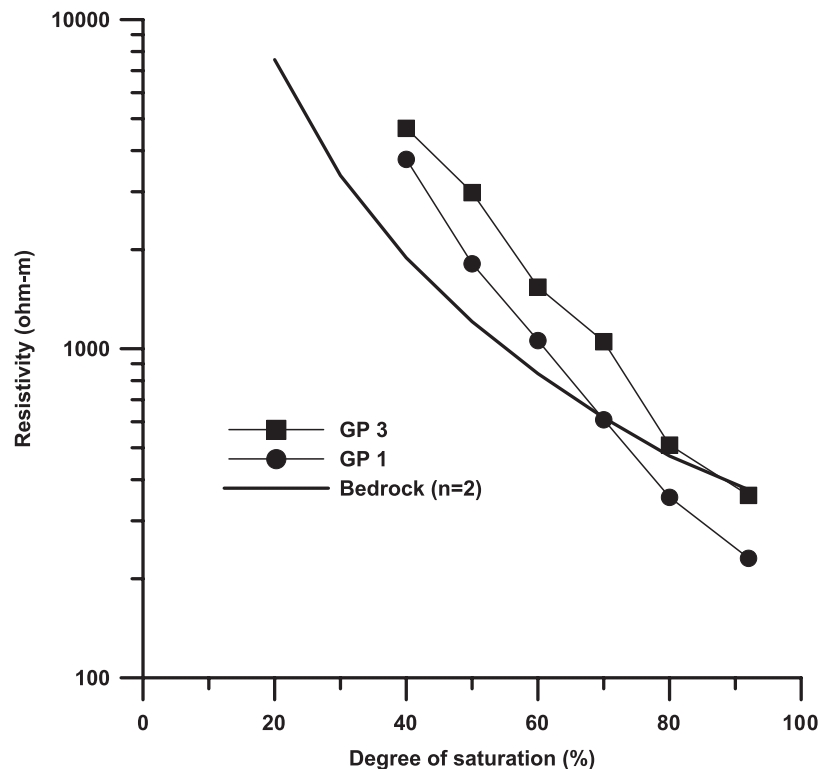


Fig. 5. Plot of real resistivity versus saturation of the pores for soil samples from GP1, GP3, and the sandstone outcrop specimen

Forward Model

User-defined properties of the finite-difference mesh in the RES2DMOD model were taken from the direct soil probe and laboratory measurements. Resistivity values for the soil and bedrock layers were set to 3,000 and 1,250 Ωm , respectively. The resistivity values were based on the results of the previous small-scale laboratory experiments for a degree of saturation of 50%. The depth of the soil–bedrock contact was defined in the model from the soil probe survey results.

Fig. 6 shows inverted tomograms of the modeled resistivity data. Topography data from surveyed electrode locations were added to the modeled datasets before solving the inversion problem. Position and elevation of all transects are to the scale of the field experiment results, as are the resistivity contour values. The model data needed to be inverted to be qualitatively compared with the inversions performed on the field geophysical datasets. The resistivity contours showed the sharpest contrast near the depth of the soil–bedrock contact in the modeled tomograms. Decrease in resistivity with depth was gradational, as the material electrical properties passed from soil to bedrock. The trend is apparent over the extent of each modeled tomogram at the soil–bedrock contact, and was assumed to represent the similar resistivity changes expected at the soil–bedrock interface in the field site.

Field Resistivity Tomography

Fig. 7 shows the inverted resistivity tomograms for each transect location in the basin. Horizontal resistivity contours were apparent in each tomogram and begin at a depth ranging from 0.55 to 1.95 m below the surface. Decreasing resistivity trends with increasing depth typically began from the top of the tabular features in each section. High-resistivity ($>3,000 \Omega\text{m}$) anomalies were apparent in each survey within 1.0 m depth below the surface, but were not

laterally extensive. In the upslope transect (A-A'), a resistivity contrast area that decreased with depth ranged in value from 1,000 to 2,000 Ωm [Fig. 7(b)]. The contrast area extended over the entire length of the transect and was located just below high ($>3,000 \Omega\text{m}$) resistivity anomalies near the ground surface.

In the downslope transect (B-B'), the resistivity contours showed the same general trend as in the upslope transect, where resistivity decreased in depth and the contours spanned the length of the transect. Resistivity values ranged from $\sim 600 \Omega\text{m}$ on the western slope to nearly 2,200 Ωm near the eastern nose [Fig. 7(b)]. Two distinct features were apparent at the bottom of the section between 22 and 24 m, and 30 and 35 m distance across the transect [Fig. 7(b)]. The features exhibited a constant resistivity of $\sim 800 \Omega$ and did not decrease with depth. The second feature was a sharp, truncated contact between the tabular resistivity trends east of the anomaly at the 35 m position.

Finally, in the axis transect [C-C'; Fig. 7(c)], resistivity ranged from 1,000 to 3,000 Ωm for the area of contrast just below the high surface anomalies across the entire transect. The resistivity trends at the intersection between the axis (C-C') and the upslope (A-A') and downslope (B-B') surveys appeared largely to agree with minor disparities between the resistivity values that result from separate inversion calculations. In general, resistivity was lowest farther upslope in the transect, and resistivity was highest downslope in the transect.

Interpretation and Discussion

Two distinct trends were similar in the resistivity contours from both the inverted forward model results and the tomograms of the field resistivity data. First, resistivity contours of between 1,000 and 2,000 Ωm were consistent that extend the length of each tomogram and were oriented directly under areas of high ($\sim 3,000 \Omega\text{m}$)

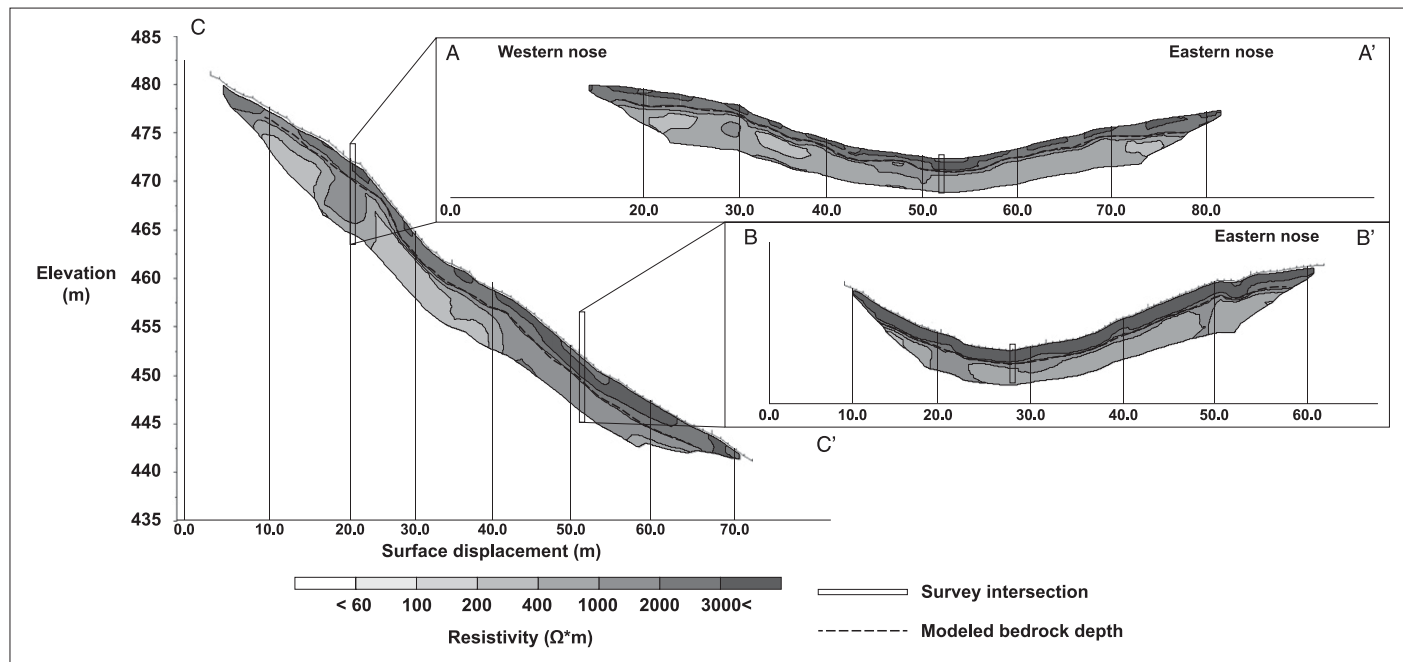


Fig. 6. Results of the forward model for each survey transect; vertical exaggeration of each section = 1.0

resistivity near the ground surface. Second, resistivity decreased gradually with depth below these contours. We interpreted the depth of the beginning of this resistivity contrast as the depth of the soil-bedrock interface in the field. Fig. 7 shows the interpreted bedrock contact for each survey line combined with nearby soil depth measurements. The uppermost resistivity contour in the decreasing-with-depth trend present in each tomogram was largely consistent with the nearby measured soil probe depths [Figs. 7(b and c)]. The interpreted depth-to-bedrock at the intersections of the survey transects remained consistent for the coinciding depths in the axis survey.

The high resistivity anomalies that occurred near the surface for all of the survey tomograms [Figs. 7(b and c)] likely represented remnant tree root networks and soil pipes (Fig. 3). An abrupt increase in bedrock depth can produce such an effect in the inversion calculation; however, it is more likely the effect of localized soil pipes or macropores created from decayed root networks. An electrical survey measurement occurring within a high-resistivity soil pipe would result in a halo of anomalously high resistivity in the surrounding unit as a product of the inversion algorithm calculation. On the other hand, results from the laboratory measurements suggest that boulders or dropstones present in the soil may portray a localized, low-resistivity anomaly within the soil much like the effect of high-resistivity anomalies caused by the remnant roots.

Sharma et al. (1997) measured an electrical resistivity of between 10^3 and 10^4 Ωm for samples of wood saturated with water. These values roughly corresponded to the $\geq 3,000$ Ωm resistivities obtained for the near-surface anomalies between 10 and 30 m and 60 and 75 m in transect A-A' (Fig. 7b). The high resistivity anomalies between the 18–22, 34–36, 46–51, and 59–63 m positions of the downslope transect (B-B') were consistent with the range in remnant root resistivity values, and they correlated to locations of high-density surface vegetation at the field site. Large piles of wet wood and stumps were scattered over the surface in the upslope area and likely extended into the subsurface beneath. The surface material was generally dry; however, the western part of the basin was thickly vegetated (Fig. 2), whereas the eastern nose was markedly less so.

The resistivity value that most closely resembled the location of the water table in GP3 agreed with the 300 Ωm value calculated for the sandstone near saturation (Fig. 5). In the modeled downslope section (B-B'), a high-resistivity anomaly between the 19- and 25-m positions at depth was met with a sharp contrast to the low resistivity values noticed around GP3 that were similar to those found in the field geophysical data. The contrasts in resistivity were noticeable in both inverted tomograms of the field and modeled datasets, and may be a result of a steep sloping of the soil–bedrock contact at this location. A 3-m-thick colluvium layer was found near borehole GP3 during the initial site investigations and digging of soil pits. The colluvium may have resulted from a prior debris flow event that scoured the bedrock in this location.

Statistical Depth Analysis

Using the interpreted depths from the inverted resistivity sections in Fig. 7, we created a grid of the soil depth distribution in the basin using the original kriging method and surveyed coordinates of electrode locations in the field. The resulting contour map of the interpreted depth-to-bedrock determined by the geophysical survey is shown in Fig. 8. Interpolation of bedrock depth between the survey lines was conducted using the same kriging procedure as with the soil probe measurements. The shallowest depths were toward the basin noses (convex topographic areas), and the deepest were downslope along the axis—similar to the trends from the point measurement survey in Fig. 4.

Interpreted bedrock depths in the contour map that were a distance away from the geophysical survey transects were interpolated using the kriging method (Deutsch and Journel 1998). Statistics of the interpolated depths compared with the depths along each transect can be plotted using a semivariogram. Figs. 9(a and b) show the variance of the soil–bedrock contact depth (y -axis) at a distance from the geophysical survey transect (“lag distance” on the x -axis). Bedrock depth variance steadily increases as the topographic trend changes from a divergent ridge and convergent valley. The variogram plot in Fig. 9(a) represents the variance in the interpreted

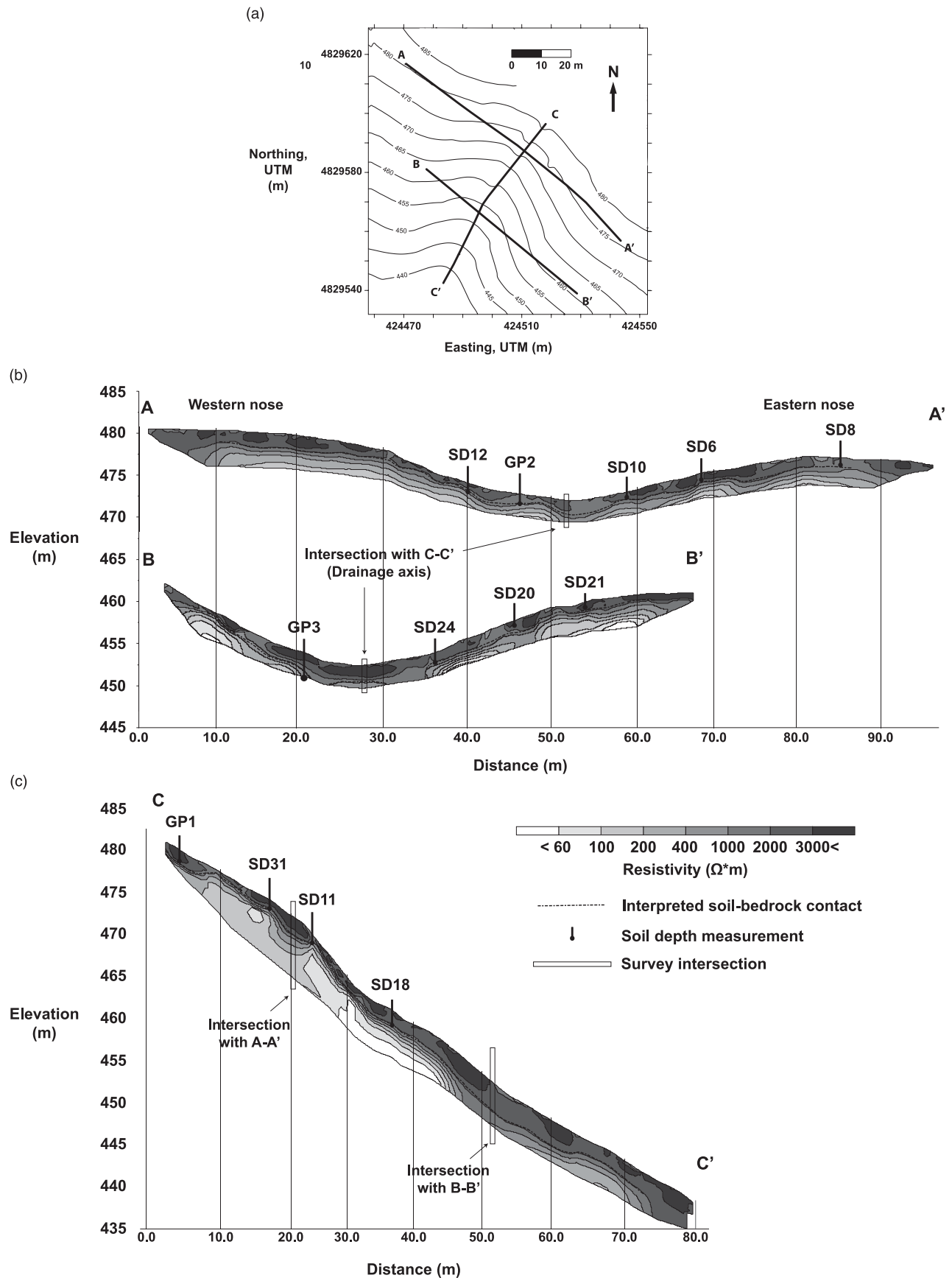


Fig. 7. Inverted resistivity tomograms for each transect location in the basin: (a) reference map showing locations of each survey transect in the basin; (b) tomograms for A-A' and B-B' transects; (c) tomogram for the C-C' transect; all maps were scaled to relate true elevation with topography in each profile; depths of the nearest soil probe and borehole measurements are shown to scale; vertical exaggeration for all maps = 1.0

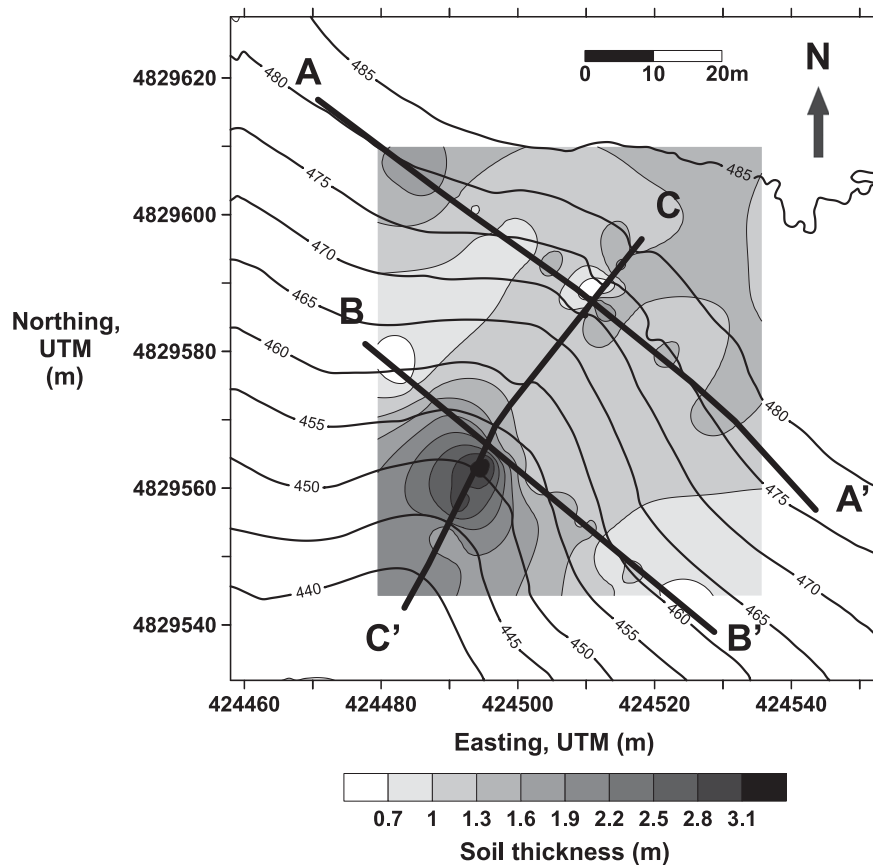


Fig. 8. Combined contour map of elevation with interpreted bedrock depth from DC survey

bedrock depth at a distance in the direction of the drainage axis (NE/SW trend). The plot in Fig. 9(b) represents the variance in interpreted bedrock depth at a distance perpendicular to the survey transects (NW/SE trend).

In the direction of the drainage axis, variance of bedrock depth started relatively low, but increased steadily until it reached its maximum (0.5 m^2) at a distance of $\geq 20 \text{ m}$ [Fig. 9(a)]. Perpendicular to the direction of the drainage axis, variance in soil depth data was sporadic and increased steadily with lag distance [Fig. 9(b)].

Fig. 10(a) shows a contour map of the difference between the kriged geophysically interpreted bedrock depth results from the resistivity survey and the measured depths from the soil probe and Geoprobe locations. The bedrock depths were most closely in agreement near the western nose of the drainage basin, and the difference in kriged bedrock depths between the two methods was greatest in the downslope area. The large difference was likely the result of resistivity anomalies in the B-B' transect that made depth interpretation difficult using our criteria.

Fig. 10(b) shows a plot comparing the measured soil probe ground-truth bedrock depths with the interpreted kriged resistivity depths at the locations of the soil probe measurements. The lateral displacement from the survey line is defined by the 2D distance perpendicular to the nearest transect in UTM coordinates. Ground-truth measurements are soil probe and Geoprobe depth locations. The difference between the interpreted and measured bedrock depths had a RMSE of 27 cm for a $\leq 16.5 \text{ m}$ distance from the survey line. Soil probe measurement locations that had a large difference between the geophysical data (SD26 and SD19) were located in the areas exhibiting large differences, as shown in Fig. 10(a). The location of probe SD19 was in the direction perpendicular to the trend of the catchment axis, where soil depth predictions vary greatest

to actual soil depths in that direction [Fig. 9(b)]. The measurement locations at SD2, SD13, and SD14 exhibited far smaller differences, and were closest to transect lines in the direction of the trend of the drainage axis. From the statistical analysis results, it is apparent that the bedrock depths can be more accurately interpolated in the direction of the drainage than perpendicular to it.

Implications and Limitations

Spurious data points, values that exhibited extreme high or low resistivity values outside the practical range in resistivities for the materials present, comprised $\sim 10\%$ of the geophysical data and were removed from each dataset in the inversions. These high measurement errors apparently resulted from the low moisture content of the subsurface materials and/or soil pipes as the result of decaying roots or animal burrows, causing a discontinuous electrical connection between the surface electrodes and surrounding soil. Boundary effects in each section also resulted where resistivity values exhibit high errors close to each survey endpoint. Resistivity contours were truncated at the boundaries of each transect in the tomograms of the field survey [Figs. 7(b and c)]. The truncation was likely the result of the influence of inversion boundary effects. Consequently, interpretations of the bedrock depth were not made west of the 10-m and east of the 86-m surface position [Fig. 7(b)]. In addition, resolution of resistivity measurements was lowest at the endpoints and the bottom of each section, resulting in discontinuous contours [Figs. 7(b and c)].

Results of the laboratory analyses of the soil and bedrock showed a decreasing difference in measured resistivity for degrees of saturation $> 70\%$ (Fig. 5). In cases in which the field saturation conditions would obscure the difference in measured resistivity between the

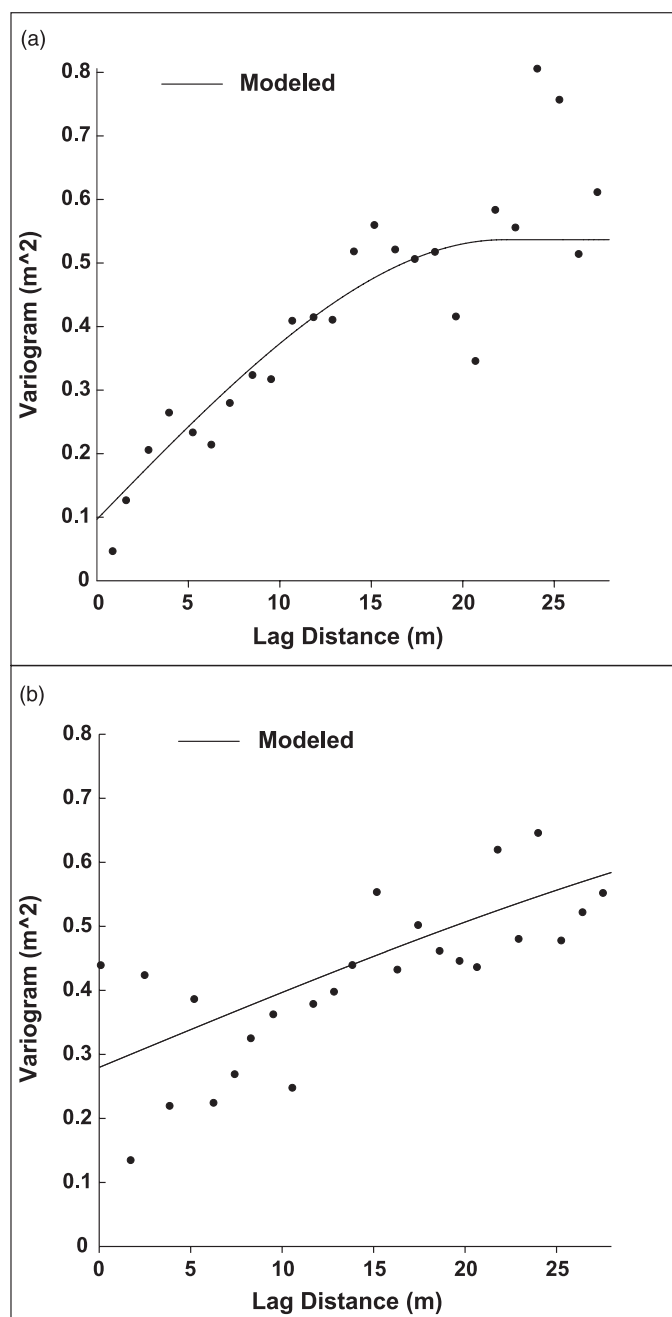


Fig. 9. Variance of soil-bedrock contact depth at a distance from the geophysical survey transect: (a) DC survey depth data with orientation in the direction of drainage axis; (b) DC survey depth data in the direction perpendicular to the drainage axis

two materials, the material boundary would be very difficult to locate using the DC resistivity method alone. In such cases, other geophysical tools may need to be applied, such as passive seismicity (Meric et al. 2007), which measures the S-wave velocities in the subsurface layers. For materials that are rich in clays, resistivity throughout the subsurface would be greatly reduced as a result of the relatively high concentration of soluble ions in the pore water (Jougnot et al. 2010). Further laboratory experimentation with these materials, such as cation exchange capacity and clay content measurements, would need to be conducted to characterize the resistivity measurements obtained in the field. During the laboratory experiments, we were unable to determine resistance values for degrees of saturation of less than ~40% as a result of the poor electrical contact with the electrodes in the experimental setup. In addition, resistivity

measurements for degrees of saturation >92% were not possible because the electrodes were mobile when in contact with the sample and lost their spacing. More robust laboratory testing measures are needed if a survey is conducted on clay-rich materials.

Limitations with the forward modeling software only allowed for a laterally constricted upslope tomogram because of the long extent of the survey transect. The endpoints for each modeled transect were also removed because the boundary effects present in each section affected the depth interpretations. In contrast to the field geophysical results, the resistivity trends with depth in the forward model tomograms did not fall below values of 400 Ωm and exhibited minor gradation with depth. This was likely caused by the assumption of a uniform resistivity value set for the bedrock (1,250 Ωm , as determined by the laboratory measurements above). In the field

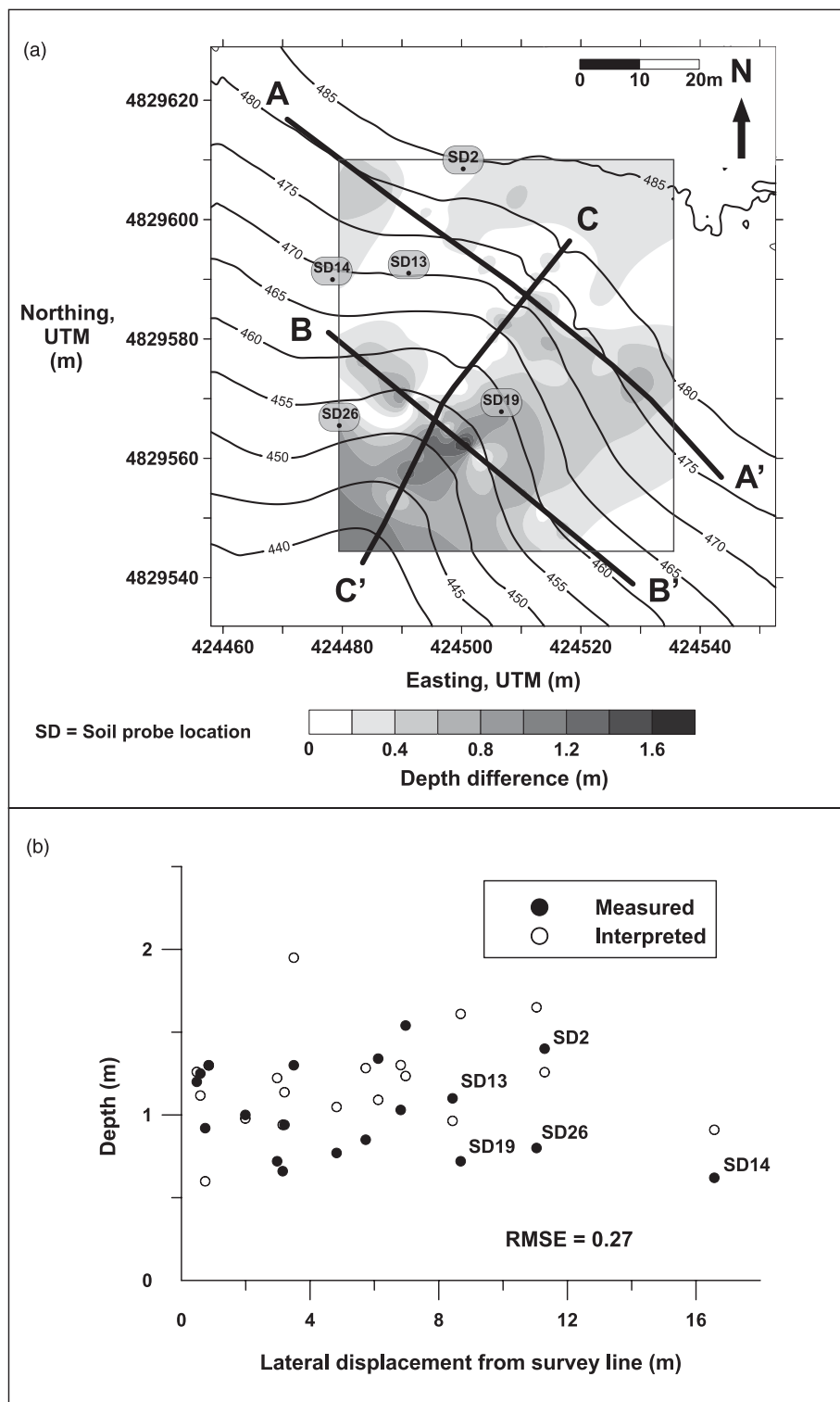


Fig. 10. Difference between ground-truth and resistivity survey data: (a) contour map of the difference in kriged, interpreted bedrock depth from the resistivity survey, and kriged data from the soil probe survey; (b) comparison plot between ground-truth bedrock depth data and the interpreted depths from resistivity modeling

site, hydrostatic conditions are likely not the case, and capillary zones are present in unconfined aquifers. The gradational decrease in resistivity with depth in each section may be attributed to an increase in saturation as a result of capillary effects resulting from the deeper water table. Other inversion techniques, such as the least-squares method with smoothing effects, would better test this

assumption (Ellis and Oldenburg 1994); but that is not the primary focus of this study.

Accurate assessment of soil thickness in zero-order drainage basins provides an important constraint for estimates of potential failure depths and landslide volumes on steep, colluvial-mantled slopes. A DC resistivity survey offers a relatively quick and nonintrusive

method for estimating the bedrock depth over laterally extensive areas compared to manual soil probing. If soil and bedrock resistivity values can be differentiated in a DC survey dataset, these data can effectively provide soil depth measurement for the area of study. Over the three days required for completion of the geophysical survey, we obtained >2,000 resistivity measurements. Hundreds of soil probe boreholes would need to be drilled to replicate the spatial density of the dataset from the resistivity survey, and small-scale features, such as the soil pipes pointed out by this study, may be missed. However, prior knowledge of the approximate bedrock depth increases the quality and resolution of the resistivity data through proper planning of electrode spacing. Employing a small number of scattered soil probe measurements alongside an extensive resistivity survey may be the most efficient means for mapping bedrock depth geometry throughout a steepland drainage basin. However, as mentioned previously, other geophysical survey techniques, such as passive seismicity (Meric et al. 2007), should be considered for this purpose when the soil is near saturation.

Conclusions

We conducted a DC resistivity survey along three transects to construct a soil thickness map of a steep, recently clear-cut, zero-order drainage basin. Point measurements of bedrock depth obtained using a soil probe were used as ground truth, to test the reliability of the resistivity method for constraining bedrock depth in the drainage basin. Measured depth-to-bedrock ranged from between 0.55 and 3.2 m at the field site. Two soil samples and one bedrock sample were taken from the field site. Electrical resistivity of the materials was tested in a laboratory for a range of 40 to 92% degree of saturation. Results from the laboratory measurements and point-measurements of bedrock depth were implemented in a forward model, to study the resistivity contrast at the soil–bedrock interface. In the model, soil and bedrock layers were defined at constant resistivity values of 3,000 and 1,250 Ωm , respectively. The resistivity values were determined from the laboratory tests at a degree of saturation of 50%. Topography and depth-to-bedrock in the model were determined from the point-measurement data at the field site. A decreasing-with-depth resistivity contrast was found at the soil–bedrock interface in the inverted tomograms of the model results. The results were used to help interpret the bedrock depths for the field resistivity data.

In the geophysical dataset, resistivity contours that exhibited a decreasing resistivity gradient with depth were apparent for each survey transect. A horizontal resistive layer of between 1,000 and 2,000 Ωm was found in each transect tomogram, and resistivity decreased in depth from this contour. The layer was interpreted as the soil–bedrock contact, based on the similar trends found from the results in the forward model. High resistivity anomalies of >3,000 Ωm were apparent near the surface of the basin, where remnant root networks and tree stumps were found in abundance. Areas with irregular topography where colluvial, well-sorted granular soil was present also exhibited relatively higher resistivity values, likely the result of the increase in pore space and low saturation level of the pores. Calculated resistivity for near-saturated sandstone was $\sim 300 \Omega\text{m}$, where a similar trend was apparent for a depth at which saturated samples were obtained from the borehole.

Kriged maps of the depths from the interpreted resistivity data were compared with those measured in the field. Both maps indicated that soil thickness was the least on the topographic noses of the basin and generally increased with distance downslope. Changes in bedrock depth in the direction of the drainage axis were correlated to within 20 m of surface distance, where variance of

bedrock depth increased steadily when comparing from convergent valleys to divergent ridges. A kriged bedrock depth map from the interpreted resistivity survey had an RMSE of 0.27 m when compared with the depths at the soil probe measurement locations taken in this study.

Acknowledgments

This work was partially funded by a grant from the U.S. Dept. of Education (P200A060133-08) and a grant from the National Science Foundation (NSF-CMMI-0855783) to N. Lu and a fellowship from the Hydrologic Science and Engineering program at Colorado School of Mines to M. S. Morse. Greg Kreimeyer, Jim Young, and John Seward of the Oregon Department of Forestry granted access to the field site in the Elliott State Forest. Brian Passerella, Damien Jougnot, Murat Kaya, and Basak Sener-Kaya of the Colorado School of Mines Department of Engineering, and Rex Baum and Andrew Ashlock of the U.S. Geological Survey provided support in the laboratory and in the field. Kevin Schmidt and William Stephenson, USGS, provided constructive reviews that strengthened the paper.

Disclaimer

Any use of trade, product, or firm names is for descriptive purposes only and does not imply endorsement by the U.S. Government.

References

- Archie, G. E. (1942). "The electrical resistivity log as an aid in determining some reservoir characteristics." *Trans. AIME*, 146(1), 54–67.
- Benda, L. (1990). "The influence of debris flows on channels and valley floors in the Oregon Coast Range, U.S.A." *Earth Surf. Process. Landf.*, 15(5), 457–466.
- Benda, L., Hassan, M. A., Church, M., and May, C. L. (2005). "Geomorphology of steepland headwaters: The transition from hillslopes to channels." *J. Am. Water Resour. Assoc.*, 41(4), 835–851.
- Bichler, A., et al. (2004). "Three-dimensional mapping of a landslide using a multi-geophysical approach: The Quesnel Forks landslide." *Landslides*, 1(1), 29–40.
- Birkeland, P. W. (1999). *Soils and geomorphology*, 3rd Ed., Oxford University Press, New York.
- Bogoslovsky, V. A., and Ogilvy, A. A. (1977). "Geophysical methods for the investigation of landslides." *Geophysics*, 42(3), 562–571.
- Brown, G. W., and Krygier, J. T. (1971). "Clear-cut logging and sediment production in the Oregon Coast Range." *Water Resour. Res.*, 7(5), 1189–1198.
- Campbell, R. (1975). "Soil slips, debris flows, and rainstorms in the Santa Monica Mountains and vicinity, southern California." *U.S. Geological Survey Professional Paper*, Vol. 851, U.S. Printing Office, Washington, DC.
- Claerbout, J. F., and Muir, F. (1973). "Robust modeling with erratic data." *Geophysics*, 38(5), 826–844.
- Dai, F. C., and Lee, C. F. (2001). "Frequency-volume relation and prediction of rainfall-induced landslides." *Eng. Geol.*, 59(3–4), 253–266.
- Deutsch, C. V., and Journel, A. G. (1998). *GSLIB: A geostatistical software library and user's guide*, 2nd Ed., Oxford University Press, London.
- Dietrich, W. E., and Dunne, T. (1978). "Sediment budget for a small catchment in mountainous terrain." *Z. Geomorphol. (Suppl.)* 29(1), 191–206.
- Dietrich, W. E., Wilson, C. J., and Reneau, S. L. (1986). "Hollows, colluviums, and landslides in soil-mantled landscapes." *Hillslope processes*, A. D. Abrahams, ed., Allen and Unwin, London, 361–388.
- Ebel, B. A., Loague, K., and Borja, R. I. (2010). "The impacts of hysteresis on variably saturated hydrologic response and slope failure." *Environ. Earth. Sci.*, 61(6), 1215–1225.
- Ebel, B. A., Loague, K., Montgomery, D. R., and Dietrich, W. E. (2008). "Physics-based continuous simulation of long-term near-surface

- hydrologic response for the Coos Bay experimental catchment." *Water Resour. Res.*, 44(1), W07417.
- Ellis, R. G., and Oldenburg, D. W. (1994). "Applied geophysical inversion." *Geophys. J. Int.*, 116(1), 5–11.
- Friedel, S., Thielen, A., and Springman, S. M. (2006). "Investigation of a slope endangered by rainfall-induced landslides using 3D resistivity tomography and geotechnical testing." *J. Appl. Geophys.*, 60(2), 100–114.
- Godt, J. G., Baum, R. L., and Lu, N. (2009). "Landsliding in partially saturated materials." *Geophys. Res. Lett.*, 36, L02403.
- Jougnot, D., Ghorbani, A., Revil, A., Leroy, P., and Cosenza, P. (2010). "Spectral induced polarization of partially saturated clay-rocks: A mechanistic approach." *Geophys. J. Int.*, 180(1), 210–224.
- Kim, J., Jeong, S., Park, S., and Sharma, J. (2004). "Influence of rainfall-induced wetting on the stability of slopes in weathered soils." *Eng. Geol.*, 75(3–4), 251–262.
- Lapenna, V., Lorenzo, P., Perrone, A., Piscitelli, S., Sdao, F., and Rizzo, E. (2003). "High-resolution geoelectrical tomographies in the study of Giarossa landslide (southern Italy)." *Bull. Eng. Geol. Environ.*, 62(3), 259–268.
- Leroy, P., Revil, A., Kemna, A., Cosenza, P., and Gorbani, A. (2008). "Spectral induced polarization of water-saturated packs of glass beads." *J. Colloid Interface Sci.*, 321(1), 103–117.
- Loke, M. H. (1999). "Rapid 2D resistivity forward modelling using the finite-difference and finite-element methods." (<http://www.abem.se/files/upload/manr2dmod.pdf>) (Oct. 1, 1999).
- Loke, M. H., and Barker, R. D. (1996). "Practical techniques for 3D resistivity surveys and data inversion." *Geophys. Prospect.*, 44(3), 499–523.
- Lovell, J. P. B. (1969). "Tye Formation; A study of proximity in turbidites." *J. Sediment. Res.*, 39(3), 935–953.
- Lu, N., and Godt, J. W. (2008). "Infinite slope stability under steady unsaturated seepage conditions." *Water Resour. Res.*, 44(11), W11404.
- Meric, O., Garambois, S., Malet, J. P., Cadet, H., Gueguen, P., and Jongmans, D. (2007). "Seismic noise-based methods for soft-rock landslide characterization." *Bull. Soc. Geol. Fr.*, 178(2), 137–148.
- Montgomery, D. R., Dietrich, W. E., Torres, R., Anderson, S. P., Heffner, J. T., and Loague, K. (1997). "Hydrologic response of a steep, unchanneled valley to natural and applied rainfall." *Water Resour. Res.*, 33(1), 91–109.
- Montgomery, D. R., Schmidt, K. M., Dietrich, W. E., and McKean, J. (2009). "Instrumental record of debris flow initiation during natural rainfall: Implications for modeling slope stability." *J. Geophys. Res.*, 114(1).
- Montgomery, D. R., Schmidt, K. M., Greenberg, H. M., and Dietrich, W. E. (2000). "Forest clearing and regional landsliding." *Geology*, 28(4), 311–314.
- Niininen, H., and Kelha, V. (1979). "Construction of a wide-range specific resistivity meter with logarithmic output." *J. Phys. E Sci. Instrum.*, 12(4), 261–263.
- Pierson, T. C. (1977). "Factors controlling debris-flow initiation on forested hillslopes in the Oregon Coast Ranges." Ph.D. thesis, Univ. of Washington, Seattle.
- Revil, A., Cathles, L. M., Losh, S., and Nunn, J. A. (1998). "Electrical conductivity in shaly sands with geophysical applications." *J. Geophys. Res.*, 103(B10), 23925–23936.
- Revil, A., and Glover, P. W. J. (1998). "Nature of surface electrical conductivity in natural sands, sandstones, and clays." *Geophys. Res. Lett.*, 25(5), 691–694.
- Revil, A., and Jougnot, D. (2008). "Diffusion of ions in unsaturated porous materials." *J. Colloid Interface Sci.*, 319(1), 226–235.
- Roering, J. J., Schmidt, K. M., Stock, J. D., Dietrich, W. E., and Montgomery, D. R. (2003). "Shallow landsliding, root reinforcement, and the spatial distribution of trees in the Oregon Coast Range." *Can. Geotech. J.*, 40(2), 237–253.
- Schmidt, K. M. (1999). "Root strength, colluvial soil depth, and colluvial transport on landslide-prone hillslopes." Ph.D. thesis, Univ. of Washington, Seattle.
- Schmidt, K. M., Roering, J. J., Stock, J. D., Dietrich, W. E., Montgomery, D. R., and Schaub, T. (2001). "The variability of root cohesion as an influence on shallow landslide susceptibility in the Oregon Coast Range." *Can. Geotech. J.*, 38(5), 995–1024.
- Schmutz, M., Guerin, R., Andrieux, P., and Maquaire, O. (2009). "Determination of the 3D structure of an earthflow by geophysical methods: The case of Super Sauze, in the French southern Alps." *J. Appl. Geophys.*, 68(4), 500–507.
- Schrott, L., and Sass, O. (2008). "Application of field geophysics in geomorphology: Advances and limitations exemplified by case studies." *Geomorphology*, 93(1–2), 55–73.
- Sharma, S. K., Shukla, S. R., and Kamala, B. S. (1997). "Studies on DC electrical resistivity of plantation grown timbers." *Holz als Roh-Werkstoff*, 55(6), 391–394 (in German).
- Sidle, R. C., and Ochiai, H. (2006). "Landslides: Processes, prediction, and land use." *Water Resour. Monog. 18*, American Geophysical Union, Washington, DC.
- Torres, R., Dietrich, W. E., Montgomery, D. R., Anderson, S. P., and Loague, K. (1998). "Unsaturated zone processes and the hydrologic response of a steep unchanneled catchment." *Water Resour. Res.*, 34(8), 1865–1879.
- Wolke, R., and Schwetlick, H. (1988). "Iteratively reweighted least squares: Algorithms, convergence analysis, and numerical comparisons." *SIAM J. Sci. Statist. Comput.*, 9(5), 907–921.
- Wu, W., and Sidle, R. C. (1995). "A Distributed slope stability model for steep forested hillslopes." *Water Resour. Res.*, 31(8), 2097–2110.